NUREG/CR-3689 Vol. III
ANL-83-85 Vol. III

NUREG/CR-3689 Vol. III
ANL-83-85 Vol. III

MATERIALS SCIENCE AND TECHNOLOGY DIVISION LIGHT-WATER-REACTOR SAFETY RESEARCH PROGRAM: QUARTERLY PROGRESS REPORT

July — September 1983

ARGONNE NATIONAL LABORATORY, ARGONNE, ILLINOIS
Operated by THE UNIVERSITY OF CHICAGO

Prepared for the Office of Nuclear Regulatory Research
U. S. NUCLEAR REGULATORY COMMISSION
under Interagency Agreement DOE 40-550-75

Argonne National Laboratory, with facilities in the states of Illinois and Idaho, is owned by the United States government, and operated by The University of Chicago under the provisions of a contract with the Department of Energy.

Available from

GPO Sales Program
Division of Technical Information and Document Control
U. S. Nuclear Regulatory Commission
Washington, D.C. 20555

and

National Technical Information Service
Springfield, Virginia 22161

NUREG/CR-3689 Vol. III
ANL-83-85 Vol. III

Distribution Code: R3

ARGONNE NATIONAL LABORATORY
9700 South Cass Avenue
Argonne, Illinois 60439

MATERIALS SCIENCE AND TECHNOLOGY DIVISION
LIGHT-WATER-REACTOR SAFETY RESEARCH PROGRAM: QUARTERLY PROGRESS REPORT
July—September 1983

Date Published: July 1984

Previous reports in this series

ANL-82-41 Vol. I	January—March 1982
ANL-82-41 Vol. II	April—June 1982
ANL-82-41 Vol. III	July—September 1982
ANL-82-41 Vol. IV	October—December 1982
ANL-83-85 Vol. I	January—March 1983
ANL-83-85 Vol. II	April—June 1983

Prepared for the Division of Engineering Technology
Office of Nuclear Regulatory Research
U. S. Nuclear Regulatory Commission
Washington, D. C. 20555
Under Interagency Agreement DOE 40-550-75

NRC FIN Nos. A2016, A2017, A2212, A2243

MATERIALS SCIENCE AND TECHNOLOGY DIVISION
LIGHT-WATER-REACTOR SAFETY RESEARCH PROGRAM: QUARTERLY PROGRESS REPORT

July-September 1983

ABSTRACT

This progress report summarizes the Argonne National Laboratory work performed during July, August, and September 1983 on water reactor safety problems. The research and development areas covered are Environmentally Assisted Cracking in Light Water Reactors, Transient Fuel Response and Fission Product Release, Clad Properties for Code Verification, and Long-Term Embrittlement of Cast Duplex Stainless Steels in LWR Systems.

NRC Fin No.	FIN Title
A2016	Transient Fuel Response and Fission Product Release
A2017	Clad Properties for Code Verification
A2212	Environmentally Assisted Cracking in Light Water Reactors
A2243	Long-Term Embrittlement of Cast Duplex Stainless Steels in LWR Systems

TABLE OF CONTENTS

MATERIALS SCIENCE AND TECHNOLOGY DIVISION
LIGHT-WATER-REACTOR SAFETY
RESEARCH PROGRAM:
QUARTERLY PROGRESS REPORT

July-September 1983

EXECUTIVE SUMMARY

I. ENVIRONMENTALLY ASSISTED CRACKING IN LIGHT WATER REACTORS[a]

Progress in this program during the current reporting period is discussed in NUREG/CR-3806 (ANL-84-36).

II. TRANSIENT FUEL RESPONSE AND FISSION PRODUCT RELEASE[b]

This chapter describes the results of analyses comparing CORSOR (semi-empirical model) and FASTGRASS-VFP (mechanistic model) predictions of fission product release for a hypothetical accident in the Surrey Nuclear Power Plant. The results presented here and in the previous quarterly report (April-June 1983) underline the danger of using empirically determined (isothermal) release rate constants to predict the integral transient release of fission products. CORSOR-predicted integral transient release depends critically on the definition of the release rate constant, i.e., the way it is determined empirically as well as the specific accident scenario upon which it is based.

---

[a] RSR FIN Budget No. A2212; RSR Contact: J. Muscara.

[b] RSR FIN Budget No. A2016; RSR Contact: G. P. Marino.

III. CLAD PROPERTIES FOR CODE VERIFICATION[c]

Zircaloy fuel cladding is susceptible to local breach-type failures during power transients in LWRs because of stresses imposed by differential thermal expansion of the fuel and cladding. In this program, the effect of stress state, strain rate, and temperature on the deformation characteristics of irradiated Zircaloy fuel cladding is being investigated to provide mechanical-property information and a failure criterion for the cladding under loading conditions conducive to pellet-cladding interaction (PCI). The information will be used in the development of codes to analyze PCI in fuel rods from power ramp experiments in test reactors, and to evaluate the susceptibility of extended-burnup fuel elements and new fuel element designs in commercial reactors to PCI failures during power transients.

Continued efforts in the TEM-HVEM examination of a brittle-type PCI-like failure of the Big Rock Point fuel cladding, produced by internal gas pressurization at 325°C, resulted in direct observations of superlattice reflections that are characteristic of Zr_3O precipitates. Because of the very weak intensity of the superlattice reflections and the complex nature of the diffraction patterns of the cell wall regions of the cold-worked material, from which most of the superlattice reflections were observed, great care was necessary in indexing the superlattice reflections. A summary of indexed diffraction patterns containing the superlattice reflections of Zr_3O precipitates is given in this report. The results show conclusively that the brittle irradiated cladding material consists of two phases, i.e., a Zr matrix (α_I phase) and a $Zr_3O_{1\pm x}$ (α_{II} phase), rather than a single α-Zr phase. This provides a sufficient basis to reevaluate the previously held premise that unirradiated and irradiated Zircaloy cladding are essentially identical materials particularly with regard to the stress corrosion cracking mechanism during pellet-cladding interaction.

Since Zircaloy cladding is strongly textured and the Burgers vector of operating dislocations is limited to an $\vec{a}$ component only, deformation of the cladding tube is highly anisotropic. Because of the mechanical anisotropy,

---

[c] RSR FIN Budget No. A2017; RSR Contact: H. H. Scott.

failure of the tube is influenced significantly by the presence of mechanical constraint in the axial direction. Without an axial constraint, the cladding tube contracts axially to compensate for the circumferential expansion. Deformation in the radial direction, i.e., wall thinning, is normally negligible. Therefore, if axial contraction is prevented (as in the case of in-reactor PCI situation) by either friction or other forms of constraint, the tube will fail with a significantly smaller diametral strain. To investigate this important effect of axial constraint on the PCI failure behavior, the mandrel expansion tests have been modified to incorporate new fixtures that provide the necessary constraint to the cladding deformation. Design, fabrication, and assembly of the fixture have been completed. Preliminary results from a mandrel expansion test on an axially constrained unirradiated Zircaloy-4 tube are described.

IV. LONG-TERM EMBRITTLEMENT OF CAST DUPLEX STAINLESS STEELS IN LWR SYSTEMS[d]

Progress in this program during the current reporting period is discussed in NUREG/CR-3857 (ANL-84-44).

---

[d] RSR FIN Budget No. A2243; RSR Contact: J. Muscara.

I. ENVIRONMENTALLY ASSISTED CRACKING IN LIGHT WATER REACTORS

Principal Investigators:
W. J. Shack, T. F. Kassner, D. S. Kupperman, T. N. Claytor,
J. Y. Park, P. S. Maiya, W. E. Ruther, and F. A. Nichols

Progress in this program during the current reporting period is discussed in NUREG/CR-3806 (ANL-84-36).

II. TRANSIENT FUEL RESPONSE AND FISSION PRODUCT RELEASE

Principal Investigator:
J. Rest

At the request of the NRC, the fission product release predictions of FASTGRASS-VFP and CORSOR were compared for the case of a PWR (Surrey Nuclear Power Plant) core under hypothetical accident conditions.

The input data for the FASTGRASS-VFP calculations were provided by Battelle Columbus Laboratories. These input data consisted of the transient temperature (in °F) and the cumulative releases (in kg) of Cs, I, Xe, and Kr for each minute after initiation of a hypothetical accident. These data were provided for each of ten radial nodes (through the whole reactor core) and two of the 24 axial sections (i.e., axial sections 10 and 20, counting down from the top of the core). The pretransient nodal inventories of fission product (in kg) used to initialize the CORSOR calculation were assumed to be the same for all radial nodes and are shown in Table 2.1.

Table 2.1. Pretransient Nodal Inventories of Fission Product (kg)

Axial Node	Cs	I	Xe	Kr
10	0.988	0.094	1.97	0.015
20	0.512	0.048	1.02	0.008

The information available for the FASTGRASS-VFP steady-state irradiation simulation is incomplete; hence, a scenario based on the H. B. Robinson fuel history was assumed for axial nodes 10 and 20 in order to initialize FASTGRASS-VFP to the same pretransient nodal inventories used in CORSOR. The fission product inventories listed in Table 2.1 correspond to FASTGRASS-VFP calculations at an average fuel temperature of 722 K and an average temperature gradient of 1000 K/cm, with fuel burnups of ~35000 and ~17500 MWd/MT for nodes 10 and 20, respectively. A grain size of 6 μm was used for both the as-irradiated and transient calculations.

Tables 2.2 and 2.3 give the transient time/temperature histories used in the FASTGRASS-VFP and CORSOR accident simulations for axial nodes 10 and 20, respectively. Temperatures for all 10 radial nodes are shown. However, only the temperatures for radial node 4 were used for the present comparison of FASTGRASS-VFP and CORSOR.

Figure 2.1 compares FASTGRASS-VFP and CORSOR predictions for (a) Xe and Cs release and (b) I release as a function of transient time for axial node 10 and radial node 4. Table 2.4 shows the fractional fission-product release results obtained for FASTGRASS-VFP and CORSOR at the end of the 42-minute transient. Figure 2.2 and Table 2.5 show the analogous results for axial node 20. In these figures and tables, the FASTGRASS-VFP predictions for Xe, Cs, and I release are shown for two values of the radial temperature gradient (0 and 1000 K/cm). The CORSOR code is insensitive to the value of the radial temperature gradient, and hence only one set of CORSOR predictions is shown in each figure and table for comparison with the FASTGRASS-VFP predictions.

The FASTGRASS-VFP results shown in Figs. 2.1 and 2.2 and Tables 2.4 and 2.5 demonstrate that Xe and I release during the hypothetical accident is strongly dependent on the value of the radial temperature gradient. The temperature gradient provides the driving force for the biased diffusion of fission gas bubbles from within the grains to the grain boundaries. The predicted I release during the hypothetical accident is affected by the value of the temperature gradient because a substantial amount of the intragranular I (atomic I as well as CsI) is transported to the grain boundaries within relatively small fission gas bubbles. On the other hand, Cs release during the hypothetical accident is less affected by the value of the temperature gradient because the majority of the intragranular Cs that is transported to the grain boundaries migrates by atomic diffusion and not within gas bubbles. Note that a grain-growth/grain-boundary-sweeping mechanism was not included in the FASTGRASS-VFP calculations. If enhanced grain growth does occur under these transient conditions (e.g., in the presence of fuel oxidation), the FASTGRASS-VFP predictions will be much less sensitive to the radial temperature gradient. (The predictions would be greater than or equal to the predictions made with the 1000 K/cm gradient.)

Table 2.2. Transient Time (min)/Temperature (°F) Histories for Axial Node 10.

Time (min)	Radial Node 1	2	3	4	5	6	7	8	9	10
114.	.834E+03	.845E+03	.840E+03	.840E+03	.849E+03	.844E+03	.835E+03	.837E+03	.790E+03	.654E+03
115.	.173E+04	.176E+04	.174E+04	.175E+04	.176E+04	.175E+04	.174E+04	.174E+04	.164E+04	.135E+04
116.	.187E+04	.189E+04	.189E+04	.188E+04	.190E+04	.189E+04	.187E+04	.187E+04	.175E+04	.142E+04
117.	.202E+04	.205E+04	.203E+04	.204E+04	.206E+04	.205E+04	.202E+04	.202E+04	.188E+04	.151E+04
118.	.219E+04	.222E+04	.220E+04	.221E+04	.223E+04	.222E+04	.219E+04	.219E+04	.202E+04	.159E+04
119.	.238E+04	.242E+04	.240E+04	.241E+04	.244E+04	.242E+04	.239E+04	.237E+04	.218E+04	.168E+04
120.	.262E+04	.268E+04	.266E+04	.267E+04	.269E+04	.267E+04	.263E+04	.260E+04	.235E+04	.177E+04
121.	.311E+04	.326E+04	.324E+04	.325E+04	.327E+04	.324E+04	.313E+04	.307E+04	.257E+04	.187E+04
122.	.376E+04	.391E+04	.390E+04	.391E+04	.390E+04	.390E+04	.379E+04	.374E+04	.294E+04	.198E+04
123.	.410E+04	.413E+04	.413E+04	.413E+04	.412E+04	.413E+04	.411E+04	.407E+04	.349E+04	.212E+04
124.	.413E+04	.413E+04	.413E+04	.413E+04	.413E+04	.413E+04	.413E+04	.410E+04	.330E+04	.229E+04
125.	.413E+04	.413E+04	.413E+04	.413E+04	.413E+04	.413E+04	.413E+04	.413E+04	.385E+04	.251E+04
126.	.413E+04	.413E+04	.413E+04	.413E+04	.413E+04	.413E+04	.413E+04	.413E+04	.393E+04	.278E+04
127.	.413E+04	.413E+04	.413E+04	.413E+04	.413E+04	.413E+04	.413E+04	.413E+04	.400E+04	.318E+04
128.	.413E+04	.413E+04	.413E+04	.413E+04	.413E+04	.413E+04	.413E+04	.413E+04	.407E+04	.351E+04
129.	.413E+04	.413E+04	.413E+04	.413E+04	.413E+04	.413E+04	.413E+04	.413E+04	.412E+04	.360E+04
130.	.413E+04	.413E+04	.413E+04	.413E+04	.413E+04	.413E+04	.413E+04	.413E+04	.413E+04	.363E+04
131.	.413E+04	.413E+04	.413E+04	.413E+04	.413E+04	.413E+04	.413E+04	.413E+04	.413E+04	.366E+04
132.	.413E+04	.413E+04	.413E+04	.413E+04	.413E+04	.413E+04	.413E+04	.413E+04	.413E+04	.369E+04
133.	.413E+04	.413E+04	.413E+04	.413E+04	.413E+04	.413E+04	.413E+04	.413E+04	.413E+04	.371E+04
134.	.413E+04	.413E+04	.413E+04	.413E+04	.413E+04	.413E+04	.413E+04	.413E+04	.413E+04	.372E+04
135.	.413E+04	.413E+04	.413E+04	.413E+04	.413E+04	.413E+04	.413E+04	.413E+04	.413E+04	.374E+04
136.	.413E+04	.413E+04	.413E+04	.413E+04	.413E+04	.413E+04	.413E+04	.413E+04	.413E+04	.375E+04
137.	.413E+04	.413E+04	.413E+04	.413E+04	.413E+04	.413E+04	.413E+04	.413E+04	.413E+04	.375E+04
138.	.413E+04	.413E+04	.413E+04	.413E+04	.413E+04	.413E+04	.413E+04	.413E+04	.413E+04	.376E+04
139.	.413E+04	.413E+04	.413E+04	.413E+04	.413E+04	.413E+04	.413E+04	.413E+04	.413E+04	.376E+04
140.	.413E+04	.413E+04	.413E+04	.413E+04	.413E+04	.413E+04	.413E+04	.413E+04	.413E+04	.376E+04
141.	.413E+04	.413E+04	.413E+04	.413E+04	.413E+04	.413E+04	.413E+04	.413E+04	.413E+04	.375E+04
142.	.413E+04	.413E+04	.413E+04	.413E+04	.413E+04	.413E+04	.413E+04	.413E+04	.413E+04	.375E+04
143.	.413E+04	.413E+04	.413E+04	.413E+04	.413E+04	.413E+04	.413E+04	.413E+04	.413E+04	.375E+04
144.	.342E+04	.342E+04	.342E+04	.342E+04	.342E+04	.342E+04	.414E+04	.413E+04	.413E+04	.381E+04
145.	.321E+04	.321E+04	.321E+04	.321E+04	.321E+04	.321E+04	.393E+04	.392E+04	.392E+04	.400E+04
146.	.374E+04	.374E+04	.374E+04	.374E+04	.374E+04	.374E+04	.374E+04	.374E+04	.374E+04	.395E+04
147.	.377E+04	.377E+04	.377E+04	.377E+04	.377E+04	.377E+04	.377E+04	.377E+04	.377E+04	.377E+04
148.	.377E+04	.377E+04	.377E+04	.377E+04	.377E+04	.377E+04	.377E+04	.377E+04	.377E+04	.377E+04
149.	.377E+04	.377E+04	.377E+04	.377E+04	.377E+04	.377E+04	.377E+04	.377E+04	.377E+04	.377E+04
150.	.376E+04	.376E+04	.376E+04	.376E+04	.376E+04	.376E+04	.376E+04	.376E+04	.376E+04	.376E+04
151.	.376E+04	.376E+04	.376E+04	.376E+04	.376E+04	.376E+04	.376E+04	.376E+04	.376E+04	.376E+04
152.	.376E+04	.376E+04	.376E+04	.376E+04	.376E+04	.376E+04	.376E+04	.376E+04	.376E+04	.376E+04
153.	.376E+04	.376E+04	.376E+04	.376E+04	.376E+04	.376E+04	.376E+04	.376E+04	.376E+04	.376E+04
154.	.376E+04	.376E+04	.376E+04	.376E+04	.376E+04	.376E+04	.376E+04	.376E+04	.376E+04	.376E+04
155.	.376E+04	.376E+04	.376E+04	.376E+04	.376E+04	.376E+04	.376E+04	.376E+04	.376E+04	.376E+04
156.	.377E+04	.377E+04	.377E+04	.377E+04	.377E+04	.377E+04	.377E+04	.377E+04	.377E+04	.377E+04

Table 2.3. Transient Time (min)/Temperature (°F) Histories for Axial Node 20

Time (min)	Radial Node 1	2	3	4	5	6	7	8	9	10
114.	.892E+03	.904E+03	.899E+03	.900E+03	.909E+03	.904E+03	.894E+03	.893E+03	.837E+03	.680E+03
115.	.184E+04	.187E+04	.186E+04	.186E+04	.188E+04	.187E+04	.185E+04	.185E+04	.172E+04	.139E+04
116.	.197E+04	.199E+04	.199E+04	.199E+04	.200E+04	.199E+04	.197E+04	.196E+04	.183E+04	.145E+04
117.	.208E+04	.211E+04	.210E+04	.210E+04	.212E+04	.211E+04	.209E+04	.208E+04	.194E+04	.152E+04
118.	.218E+04	.221E+04	.220E+04	.220E+04	.222E+04	.221E+04	.219E+04	.217E+04	.204E+04	.158E+04
119.	.227E+04	.230E+04	.229E+04	.229E+04	.230E+04	.230E+04	.228E+04	.226E+04	.213E+04	.165E+04
120.	.236E+04	.239E+04	.238E+04	.238E+04	.239E+04	.238E+04	.237E+04	.234E+04	.221E+04	.173E+04
121.	.245E+04	.247E+04	.247E+04	.247E+04	.248E+04	.247E+04	.245E+04	.243E+04	.228E+04	.180E+04
122.	.253E+04	.256E+04	.255E+04	.255E+04	.256E+04	.255E+04	.254E+04	.250E+04	.236E+04	.187E+04
123.	.261E+04	.264E+04	.263E+04	.264E+04	.264E+04	.264E+04	.262E+04	.258E+04	.243E+04	.193E+04
124.	.270E+04	.272E+04	.271E+04	.272E+04	.272E+04	.272E+04	.270E+04	.266E+04	.249E+04	.198E+04
125.	.278E+04	.280E+04	.280E+04	.280E+04	.280E+04	.279E+04	.277E+04	.273E+04	.256E+04	.203E+04
126.	.286E+04	.288E+04	.288E+04	.288E+04	.288E+04	.287E+04	.285E+04	.280E+04	.263E+04	.208E+04
127.	.294E+04	.296E+04	.296E+04	.296E+04	.296E+04	.295E+04	.293E+04	.288E+04	.269E+04	.213E+04
128.	.302E+04	.304E+04	.304E+04	.304E+04	.305E+04	.303E+04	.301E+04	.295E+04	.276E+04	.218E+04
129.	.310E+04	.313E+04	.312E+04	.313E+04	.313E+04	.311E+04	.308E+04	.302E+04	.282E+04	.223E+04
130.	.319E+04	.321E+04	.321E+04	.321E+04	.321E+04	.319E+04	.316E+04	.309E+04	.289E+04	.229E+04
131.	.327E+04	.330E+04	.329E+04	.329E+04	.329E+04	.327E+04	.324E+04	.317E+04	.295E+04	.232E+04
132.	.336E+04	.338E+04	.338E+04	.338E+04	.337E+04	.336E+04	.332E+04	.324E+04	.302E+04	.237E+04
133.	.345E+04	.347E+04	.347E+04	.346E+04	.346E+04	.344E+04	.340E+04	.331E+04	.308E+04	.242E+04
134.	.354E+04	.356E+04	.355E+04	.355E+04	.354E+04	.352E+04	.348E+04	.339E+04	.315E+04	.247E+04
135.	.362E+04	.364E+04	.364E+04	.363E+04	.362E+04	.360E+04	.355E+04	.346E+04	.321E+04	.252E+04
136.	.371E+04	.372E+04	.372E+04	.372E+04	.370E+04	.369E+04	.363E+04	.353E+04	.328E+04	.257E+04
137.	.379E+04	.380E+04	.380E+04	.379E+04	.378E+04	.375E+04	.370E+04	.360E+04	.334E+04	.261E+04
138.	.386E+04	.388E+04	.387E+04	.387E+04	.385E+04	.382E+04	.377E+04	.366E+04	.339E+04	.266E+04
139.	.393E+04	.394E+04	.394E+04	.393E+04	.391E+04	.389E+04	.383E+04	.372E+04	.345E+04	.270E+04
140.	.399E+04	.400E+04	.400E+04	.399E+04	.397E+04	.394E+04	.389E+04	.378E+04	.351E+04	.274E+04
141.	.405E+04	.406E+04	.405E+04	.404E+04	.403E+04	.400E+04	.395E+04	.384E+04	.356E+04	.279E+04
142.	.410E+04	.411E+04	.410E+04	.409E+04	.407E+04	.405E+04	.400E+04	.389E+04	.362E+04	.283E+04
143.	.413E+04	.413E+04	.413E+04	.412E+04	.411E+04	.409E+04	.405E+04	.395E+04	.368E+04	.289E+04
144.	.413E+04	.413E+04	.413E+04	.413E+04	.413E+04	.412E+04	.410E+04	.401E+04	.377E+04	.297E+04
145.	.392E+04	.392E+04	.392E+04	.392E+04	.392E+04	.392E+04	.391E+04	.388E+04	.397E+04	.336E+04
146.	.374E+04	.374E+04	.374E+04	.374E+04	.374E+04	.374E+04	.374E+04	.374E+04	.395E+04	.374E+04
147.	.377E+04	.377E+04	.377E+04	.377E+04	.377E+04	.377E+04	.377E+04	.377E+04	.377E+04	.377E+04
148.	.377E+04	.377E+04	.377E+04	.377E+04	.377E+04	.377E+04	.377E+04	.377E+04	.377E+04	.377E+04
149.	.377E+04	.377E+04	.377E+04	.377E+04	.377E+04	.377E+04	.377E+04	.377E+04	.377E+04	.377E+04
150.	.376E+04	.376E+04	.376E+04	.376E+04	.376E+04	.376E+04	.376E+04	.376E+04	.376E+04	.376E+04
151.	.376E+04	.376E+04	.376E+04	.376E+04	.376E+04	.376E+04	.376E+04	.376E+04	.376E+04	.376E+04
152.	.376E+04	.376E+04	.376E+04	.376E+04	.376E+04	.376E+04	.376E+04	.376E+04	.376E+04	.376E+04
153.	.376E+04	.376E+04	.376E+04	.376E+04	.376E+04	.376E+04	.376E+04	.376E+04	.376E+04	.376E+04
154.	.376E+04	.376E+04	.376E+04	.376E+04	.376E+04	.376E+04	.376E+04	.376E+04	.376E+04	.376E+04
155.	.376E+04	.376E+04	.376E+04	.376E+04	.376E+04	.376E+04	.376E+04	.376E+04	.376E+04	.376E+04
156.	.377E+04	.377E+04	.377E+04	.377E+04	.377E+04	.377E+04	.377E+04	.377E+04	.377E+04	.377E+04

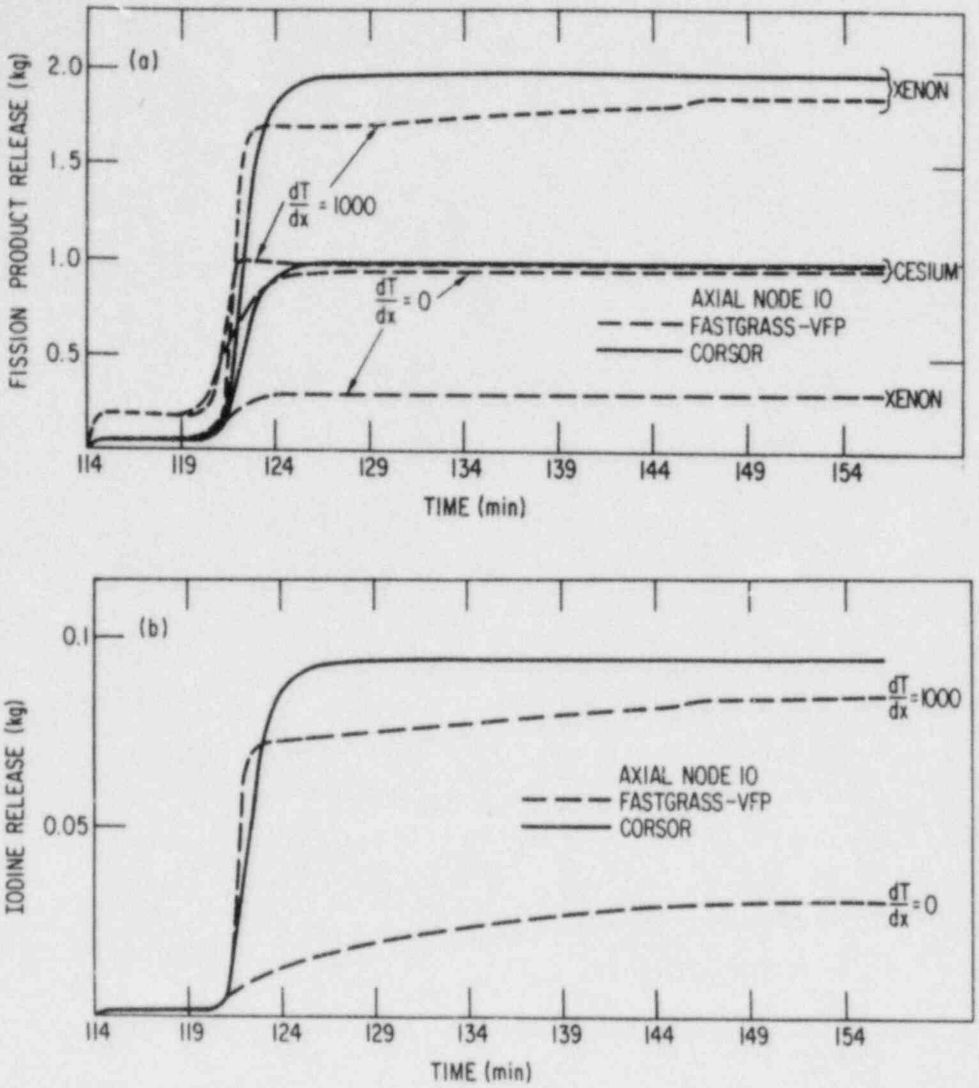

Fig. 2.1. Comparison of FASTGRASS-VFP and CORSOR Predictions for (a) Xe and Cs and (b) I Release at Axial Node 10 during a Hypothetical Accident, for Two Values of the Radial Temperature Gradient dT/dx (K/cm).

Table 2.4. Predicted Fission Product Release at End of 42-min Transient for Axial Node 10 and Radial Node 4

		Fission Product Release (%)		
	TGrad (K/cm)	Xe	Cs	I
FASTGRASS-VFP	0	9.4	82.7	15.8
	1000	80.3	100.0	68.2
CORSOR	--	100.0	99.8	100.0

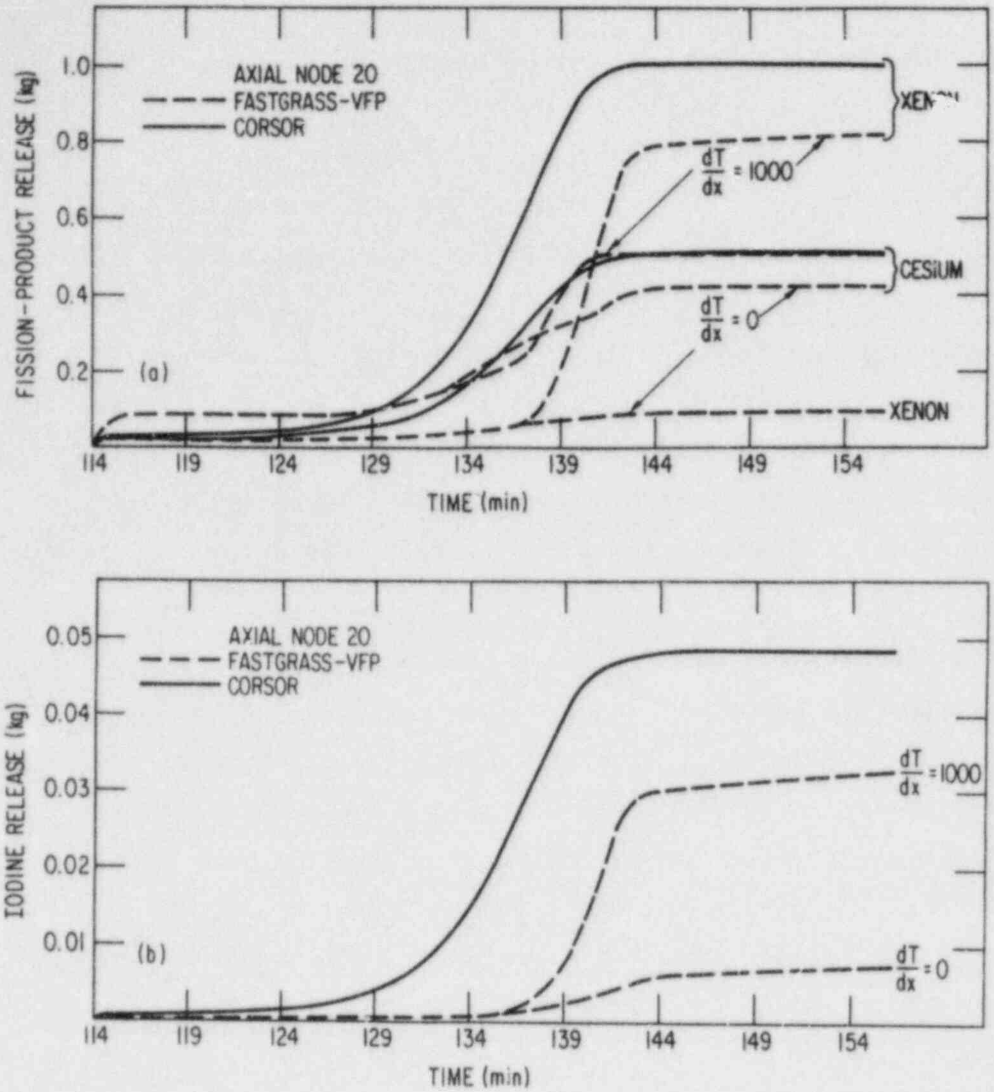

Fig. 2.2. Comparison of FASTGRASS-VFP and CORSOR Predictions for (a) Xe and Cs and (b) I Release at Axial Node 20 during a Hypothetical Accident, for Two Values of the Radial Temperature Gradient dT/dx (K/cm).

Table 2.5. Predicted Fission Product Release at End of 42-min Transient for Axial Node 20 and Radial Node 4

		Fission Product Release (%)		
	TGrad (K/cm)	Xe	Cs	I
FASTGRASS-VFP	0	9.4	82.7	15.8
	1000	80.3	100.0	68.2
CORSOR	--	100.0	99.8	100.0

In general, for temperature gradients of <1000 K/cm, FASTGRASS-VFP predicts smaller releases of I and Xe during the hypothetical accident than does the CORSOR code. Whereas CORSOR predicted a release of 100% of both the Xe and the I from axial nodes 10 and 20 during the accident, FASTGRASS predicted I releases ranging from 16 to 90% and Xe releases ranging from 10 to 94%, depending on the radial temperature gradient (see Tables 2.4 and 2.5). Note that the maximum fuel temperatures in nodes 10 and 20 were substantially below the UO_2 melting temperature (see Tables 2.2 and 2.3). In addition, as shown in Tables 2.2 and 2.3, the temperature gradient within radial node 4 was ~0 K/cm. However, the radial temperature gradient did increase to a value of several thousand K/cm toward the surface of the fuel (radial nodes 9 and 10; see Tables 2.2 and 2.3).

In the present study, FASTGRASS-VFP predicted smaller integral releases than did CORSOR for temperature gradients of <1000 K/cm; in contrast, a previous comparison indicated that isothermal release rate constants predicted by FASTGRASS-VFP tended to be, for the most part, larger than those predicted by CORSOR, and thus, larger than the experimentally determined values. This apparent inconsistency underscores the danger of using empirically determined (isothermal) release rate constants to predict integral transient release of fission products. As was pointed out in Ref. 1, the integral transient release predicted by the NUREG-0772 correlation depends critically on the definition of the release rate constants (i.e., the way they are determined empirically as well as the specific accident scenario upon which they are based). For example, the fractional fission product release predicted by FASTGRASS-VFP (Fig. 1 in Ref. 1) agrees with the ORNL data much better than FASTGRASS-VFP-predicted release rate constants agree with NUREG-0772 (Fig. 3 of Ref. 1).

Figures 2.1(a) and 2.2(a) and Tables 2.4 and 2.5 show that, in general, FASTGRASS-VFP predictions of Cs release are in reasonable agreement with CORSOR predictions. However, during the early phase of the accident, FASTGRASS-VFP tends to predict greater Cs release than does CORSOR (see Figs. 2.1(a) and 2.2(a)). The fact that FASTGRASS-VFP tends to predict greater Cs release than CORSOR has already been established[1].

The reason for this, as discussed in Ref. 1, is that FASTGRASS-VFP uses a Cs diffusion coefficient that is orders of magnitude greater than the diffusion coefficient for Xe. Thus, the rate at which Cs is predicted to be released from the fuel is greater than for I and Xe. This diffusion coefficient for Cs is based on the experimental results of Oi and Takagi.[2] If it is assumed that atomic Cs diffuses at about the same rate as Xe and I, then the FASTGRASS-predicted release rate constants for Cs will be in reasonable agreement (i.e. similar to the Xe and I results) with the NUREG-0772 results shown in Fig. 3 of Ref. 1. At temperatures greater than ~1200 K, the NUREG-0772 release-rate-constant curves for I, Xe, and Cs are identical. An extensive assessment of Cs diffusion rates in solid UO_2 is currently in progress.

Finally, the series of ORNL transient fission product release tests and the SASHA tests, which were used as the basis of the NUREG-0772 correlation, were conducted in a steam environment. The steam can change fuel stoichiometry and can subsequently affect fission product release. Theoretical models describing the effects of a steam environment and fuel liquefaction on fission product release are not currently included in FASTGRASS. Models for these processes are currently under development and will be included in a future version of FASTGRASS-VFP.

References for Chapter II

1. J. Rest and M. Piasecka, "Comparison of FASTGRASS Predictions for Fission Product Release Rate Constants with NUREG-0772," personal communication to L. Chan, USNRC (June 23, 1983).
2. N. Oi and J. Takagi, Diffusion of Non-Gaseous Fission Products in UO_2 Single Crystals, Z. Naturforsch. 19A, 1331 (1964).

III. CLAD PROPERTIES FOR CODE VERIFICATION

Principal Investigators:
H. M. Chung, F. L. Yaggee, and T. F. Kassner

The Zircaloy cladding on fuel rods in light-water-cooled reactors is susceptible to local breach-type failures, commonly known as pellet-cladding interaction (PCI) failures, during power transients after the fuel has achieved sufficiently high burnup. As a result of the high burnup, the gap between the UO_2 fuel pellets and the cladding is closed and highly localized stress is believed to be imposed on the cladding by differential thermal expansion of the cracked fuel and cladding during power transients. In addition to the localized stress, a high-burnup fuel cladding is also characterized by high-density radiation-induced defects (RID), mechanical constraints imposed by pellet-cladding friction, compositional changes (e.g., oxygen and hydrogen uptake associated with in-service corrosion), and geometrical changes due to creep-down and bowing. It is possible that synergistic effects involving more than one of the above factors influence the deformation and fracture of the in-reactor fuel cladding, e.g., strain aging associated with impurity or alloying elements, irradiation- or stress-induced segregation of the elements and subsequent formation of non-equilibrium phases. Although mechanisms of stress-corrosion cracking (SCC) associated with volatile fission products such as I and liquid-metal embrittlement (LME) associated with an element such as Cd have been well established for local breach-type failures of irradiated and unirradiated Zircaloy cladding under out-of-reactor simulation conditions, conclusive evidence of these processes is not yet available for in-reactor PCI failures. Consequently, to provide a better understanding of the PCI phenomenon, we have undertaken a mechanistic study of the deformation and fracture behavior of actual power-reactor fuel cladding, discharged after a high burnup.

In this program, the effect of temperature, strain rate, and stress localization on the deformation and fracture characteristics of Zircaloy cladding from spent-fuel rods is being investigated by means of internal gas-pressurization and mandrel-loading experiments in the absence of simulated fission product species. The deformed and fractured specimens of spent-fuel cladding are then being examined by optical microscopy, scanning electron microscopy (SEM), transmission electron microscopy (TEM), and and high-voltage electron microscopy (HVEM). The results of microstructural and fracture-property investigations will be used to develop a failure criterion for the cladding under PCI-type loading conditions. The information will be incorporated into fuel performance codes, which can be used to evaluate the susceptibility of extended-burnup fuel elements in commercial reactors to PCI failures during power transients in later cycles, and to evaluate cladding performance and reliability in new fuel-element designs. An optimization of either cladding fabrication or power ramp procedure to minimize cladding failures would result in a significant decrease in radiation exposure of plant personnel due to background and airborne radioactivity as well as an extension of core life in terms of allowable off-gas radioactivity.

A. TEM-HVEM Analysis of Zr_3O Precipitates (H. M. Chung)

1. Introduction

In continuation of the previously reported[1,2] efforts to characterize the Zr_3O precipitates that were correlated with the PCI-like, brittle-type failures of the Big Rock Point and H. B. Robinson reactor spent-fuel cladding, thin-foil specimens obtained from tubes that failed in a brittle-type manner were examined further by TEM and HVEM. In this report, TEM-HVEM diffraction patterns containing superlattice reflections of the ordered Zr-oxygen phase of Zr_3O are summarized.

2. Tabulation of the Zr_3O Superlattice Reflections

Table 3.1 lists superlattice reflections of the Zr_3O phase with interplanar spacings of >0.55 Å. The interplanar spacings were calculated on the basis of space group $P6_322$ and lattice constants of $a_o = 5.625$ Å and $c_o = 5.193$ Å.[3]

TABLE 3.1. Summary of Calculated[a] Interplanar Spacings of Zr_3O Phase

$hk\ell$	$h^2 + hk + k^2$	ℓ^2	$d_{hk\ell}$ (Å)	Superlattice Reflection[b]
001	0	1	5.195	
$100, 1\bar{1}0$	1	0	4.885	x
$101, 1\bar{1}1$	1	1	3.559	x
$110, 2\bar{1}0$	3	0	2.821	
002	0	4	2.598	
$111, 2\bar{1}1$	3	1	2.475	
200	4	0	2.443	x
$102, 1\bar{1}2$	1	4	2.295	x
$201, 2\bar{2}1$	4	1	2.210	x
$112, 2\bar{1}2$	3	4	1.912	
$210, 3\bar{1}0, 3\bar{2}0$	7	0	1.846	x
$202, 2\bar{2}2$	4	4	1.779	x
$211, 3\bar{1}1, 3\bar{2}1$	7	1	1.739	x
003	0	9	1.732	
$103, 1\bar{1}3$	1	9	1.632	x
$300, 3\bar{3}0$	9	0	1.628	
$301, 3\bar{3}1$	9	1	1.553	
$212, 3\bar{1}2, 3\bar{2}2$	7	4	1.505	x
$113, 2\bar{1}3$	3	9	1.478	
$203, 2\bar{2}3$	4	9	1.413	x
$220, 4\bar{2}0$	12	0	1.410	
$302, 3\bar{3}2$	9	4	1.380	
$221, 4\bar{2}1$	12	1	1.361	
$310, 4\bar{1}0, 4\bar{3}0$	13	0	1.355	x
$311, 4\bar{1}1, 4\bar{3}1$	13	1	1.311	x
004	0	16	1.299	
$213, 3\bar{1}3, 3\bar{2}3$	7	9	1.263	x
$104, 1\bar{1}4$	1	16	1.255	x
$222, 4\bar{2}2$	12	4	1.239	

TABLE 3.1. (Contd.)

$hk\ell$	$h^2 + hk + k^2$	ℓ^2	$d_{hk\ell}$(Å)	Superlattice Reflection^b
400,440	16	0	1.221	x
312,4$\bar{1}$2,4$\bar{3}$2	13	4	1.201	x
401,4$\bar{4}$1	16	1	1.189	x
303,3$\bar{3}$3	9	9	1.186	
114,2$\bar{1}$4	3	16	1.182	
204,2$\bar{2}$4	4	16	1.147	x
320,5$\bar{2}$0,5$\bar{3}$0	19	0	1.121	x
402,4$\bar{4}$2	16	4	1.105	x
321,5$\bar{2}$1,5$\bar{3}$1	19	1	1.096	x
223,4$\bar{2}$3	12	9	1.093	
313,4$\bar{1}$3,4$\bar{3}$3	13	9	1.070	x
410,5$\bar{1}$0,5$\bar{4}$0	21	0	1.065	
214,3$\bar{1}$4,3$\bar{2}$4	7	16	1.062	x
411,5$\bar{1}$1,5$\bar{4}$1	21	1	1.044	
005	0	25	1.039	
322,5$\bar{2}$2,5$\bar{3}$2	19	4	1.029	x
105,1$\bar{1}$5	1	25	1.016	x
304,3$\bar{3}$4	9	16	1.015	
403,4$\bar{4}$3	16	9	0.998	x
412,5$\bar{1}$2,5$\bar{4}$2	21	4	0.985	
500,5$\bar{5}$0	25	0	0.977	x
115,2$\bar{1}$5	3	25	0.975	
501,5$\bar{5}$1	25	1	0.960	x
205,2$\bar{2}$5	4	25	0.956	x
224,4$\bar{2}$4	12	16	0.955	
323,5$\bar{2}$3,5$\bar{3}$3	19	9	0.941	x
330,6$\bar{3}$0	27	0	0.940	
314,4$\bar{1}$4,4$\bar{3}$4	13	16	0.937	x
331,6$\bar{3}$1	27	1	0.926	

TABLE 3.1. (Contd.)

$hk\ell$	$h^2 + hk + k^2$	ℓ^2	$d_{hk\ell}$(Å)	Superlattice Reflection[b]
$420, 6\bar{2}0, 6\bar{4}0$	28	0	0.923	x
$502, 5\bar{5}2$	25	4	0.914	x
$421, 6\bar{2}1, 6\bar{4}1$	28	1	0.909	x
$413, 5\bar{1}3, 5\bar{4}3$	21	9	0.906	
$215, 3\bar{1}5, 3\bar{2}5$	7	25	0.905	x
$404, 4\bar{4}4$	16	16	0.889	x
$332, 6\bar{3}2$	27	4	0.884	
$510, 6\bar{1}0, 6\bar{5}0$	31	0	0.877	x
$305, 3\bar{3}5$	9	25	0.876	
$422, 6\bar{2}2.6\bar{4}2$	28	4	0.870	x
$511, 6\bar{1}1, 6\bar{5}1$	31	1	0.865	x
006	0	36	0.865	
$106, 1\bar{1}6$	1	36	0.852	x
$503, 5\bar{5}3$	25	9	0.851	x
$324, 5\bar{2}4, 5\bar{3}4$	19	16	0.848	x
$225, 4\bar{2}5$	12	25	0.836	
$512, 6\bar{1}2, 6\bar{5}2$	31	4	0.831	x
$333, 6\bar{3}3$	27	9	0.826	
$116, 2\bar{1}6$	3	36	0.828	
$414, 5\bar{1}4, 5\bar{4}4$	21	16	0.824	
$315, 4\bar{1}5, 4\bar{3}5$	13	25	0.824	x
$206, 2\bar{2}6$	4	36	0.816	x
$600, 6\bar{6}0$	36	0	0.814	
$423, 6\bar{2}3, 6\bar{4}3$	28	9	0.814	x
$601, 6\bar{6}1$	36	1	0.804	
$430, 7\bar{3}0, 7\bar{4}0$	37	0	0.803	x
$431, 7\bar{3}1, 7\bar{4}1$	37	1	0.793	x
$405, 4\bar{4}5$	16	25	0.791	x
$216, 3\bar{1}6, 3\bar{2}6$	7	36	0.783	x

TABLE 3.1. (Contd.)

$hk\ell$	$h^2 + hk + k^2$	ℓ^2	$d_{hk\ell}$ (Å)	Superlattice Reflection[b]
$513, 6\bar{1}3, 6\bar{5}3$	31	9	0.782	x
$520, 7\bar{2}0$	39	0	0.782	
$504, 5\bar{5}4$	25	16	0.781	x
$602, 6\bar{6}2$	36	4	0.777	
$521, 7\bar{2}1$	39	1	0.774	
$432, 7\bar{3}2, 7\bar{4}2$	37	4	0.767	x
$325, 5\bar{2}5, 5\bar{3}5$	19	25	0.762	x
$306, 3\bar{3}6$	9	36	0.762	
$334, 6\bar{3}4$	27	16	0.761	
$522, 7\bar{2}2$	39	4	0.749	
$610, 7\bar{1}0, 7\bar{6}0$	43	0	0.745	x
$415, 5\bar{1}5, 5\bar{4}5$	21	25	0.744	
$611, 7\bar{1}1, 7\bar{6}1$	43	1	0.737	x
$603, 6\bar{6}3$	36	9	0.736	
$107, 1\bar{1}7$	1	49	0.734	x
$316, 4\bar{1}6, 4\bar{3}6$	13	36	0.729	x
$433, 7\bar{3}3, 7\bar{4}3$	37	9	0.728	x
$514, 6\bar{1}4, 6\bar{5}4$	31	16	0.727	x
$117, 2\bar{1}7$	3	49	0.717	
$612, 7\bar{1}2, 7\bar{6}2$	43	4	0.716	x
$523, 7\bar{2}3$	39	9	0.713	
$505, 5\bar{5}5$	25	25	0.712	x
$207, 2\bar{2}7$	4	49	0.710	x
$440, 8\bar{4}0$	48	0	0.705	
$441, 8\bar{4}1$	48	1	0.698	
$700, 530, 7\bar{7}0, 8\bar{3}0, 8\bar{5}0$	49	0	0.697	x
$335, 6\bar{3}5$	27	25	0.697	
$425, 6\bar{2}5, 6\bar{4}5$	28	25	0.690	x
$604, 6\bar{6}4$	36	16	0.690	

TABLE 3.1. (Contd.)

$hk\ell$	$h^2 + hk + k^2$	ℓ^2	$d_{hk\ell}$ (Å)	Superlattice Reflection[b]
701,531,7$\bar{7}$1, 8$\bar{3}$1,8$\bar{5}$1	49	1	0.690	x
217,3$\bar{1}$7,3$\bar{2}$7	7	49	0.688	x
326,5$\bar{2}$6,5$\bar{3}$6	19	36	0.685	x
613,7$\bar{1}$3,7$\bar{6}$3	43	9	0.684	x
434,7$\bar{3}$4,7$\bar{4}$4	37	16	0.683	x
442,8$\bar{4}$2	48	4	0.680	
620,8$\bar{2}$0	52	0	0.677	x
621,8$\bar{2}$1	52	1	0.676	x
307,3$\bar{3}$7	9	49	0.675	
702,532,7$\bar{7}$2, 8$\bar{3}$2,8$\bar{5}$2	49	4	0.674	x
416,5$\bar{1}$6,5$\bar{4}$6	21	36	0.672	
515,6$\bar{1}$5,6$\bar{5}$5	31	25	0.670	x
524,7$\bar{2}$4	39	16	0.670	
227,4$\bar{2}$7	12	49	0.662	
443,8$\bar{4}$3	48	9	0.653	
622,8$\bar{2}$2	52	4	0.653	x
317, 4$\bar{1}$7,4$\bar{3}$7	13	49	0.651	x
506,5$\bar{5}$6	25	36	0.648	x
703,533,7$\bar{7}$3, 8$\bar{3}$3,8$\bar{5}$3	49	9	0.647	x
710,8$\bar{1}$0,8$\bar{7}$0	57	0	0.647	x
614,7$\bar{1}$4,7$\bar{6}$4	43	16	0.646	x
108,1$\bar{1}$8	1	64	0.643	x
711,8$\bar{1}$1	57	1	0.640	x
605,6$\bar{6}$5	36	25	0.640	
435,7$\bar{3}$5,7$\bar{4}$5	37	25	0.635	x
407,4$\bar{4}$7	16	49	0.634	x
118,2$\bar{1}$8	3	64	0.633	
623,8$\bar{2}$3	52	9	0.631	x

TABLE 3.1. (Contd.)

$hk\ell$	$h^2 + hk + k^2$	ℓ^2	$d_{hk\ell}$(Å)	Superlattice Reflection[b]
426,$6\bar{2}6$,$6\bar{4}6$	28	36	0.631	x
525,$7\bar{2}5$	39	25	0.625	
712,$8\bar{1}2$,$8\bar{7}2$	57	4	0.625	x
540,$9\bar{4}0$,$9\bar{5}1$	61	0	0.625	x
541,$9\bar{4}1$,$9\bar{5}1$	61	1	0.619	x
516,$6\bar{1}6$,$6\bar{5}6$	31	36	0.615	x
327,$5\bar{2}7$,$5\bar{3}7$	19	49	0.618	x
704,534,$7\bar{7}4$, $8\bar{3}4$,$8\bar{5}4$	49	16	0.613	x
630,$9\bar{3}0$,$9\bar{6}0$	63	0	0.613	
218,$3\bar{1}8$,$3\bar{2}8$	7	64	0.613	x
800,$8\bar{8}0$	64	0	0.610	x
631,$9\bar{3}1$,$9\bar{6}1$	63	1	0.609	
417,$5\bar{1}7$,$5\bar{4}7$	21	49	0.609	
713,$8\bar{1}3$,$8\bar{7}3$	57	9	0.604	x
542,$9\bar{4}2$,$9\bar{5}2$	61	4	0.608	x
619,$7\bar{1}5$,$7\bar{6}5$	43	25	0.604	x
801,$8\bar{8}1$	64	1	0.606	x
624,$8\bar{2}4$	52	16	0.599	x
632,$9\bar{3}2$,$9\bar{6}2$	63	4	0.597	
720,$9\bar{2}0$	67	0	0.596	x
721,$9\bar{2}1$	67	1	0.591	x
507,$5\bar{5}7$	25	49	0.590	x
802,$8\bar{8}2$	64	4	0.592	x
337,$6\bar{3}7$	27	49	0.582	
543,$9\bar{4}3$,$9\bar{5}3$	61	9	0.587	x
436,$7\bar{3}6$,$7\bar{4}6$	37	36	0.588	x
722,$9\bar{2}2$	67	4	0.580	x
526,$7\bar{2}6$	39	36	0.579	

TABLE 3.1. (Contd.)

$hk\ell$	$h^2 + hk + k^2$	ℓ^2	$d_{hk\ell}$ (Å)	Superlattice Reflection[b]
$633, 9\bar{3}3, 9\bar{6}3$	63	9	0.578	
$427, 6\bar{2}7, 6\bar{4}7$	28	49	0.578	x
$705, 7\bar{7}5, 535,$ $8\bar{3}5, 8\bar{5}5$	49	25	0.578	x
$109, 1\bar{1}9$	1	81	0.573	x
$810, 9\bar{1}0$	73	0	0.572	x
$714, 8\bar{1}4, 8\bar{7}4$	57	16	0.577	x
$811, 9\bar{1}1$	73	1	0.568	x
$517, 6\bar{1}7, 6\bar{5}7$	31	49	0.565	x
$625, 8\bar{2}5$	52	25	0.566	x
$616, 7\bar{1}6, 7\bar{6}6$	43	36	0.563	x
$544, 9\bar{4}4$	61	16	0.562	x
$723, 9\bar{2}3$	67	9	0.562	x
$640, 10\bar{4}0, 10\bar{6}0$	76	0	0.560	x
$641, 10\bar{4}1, 10\bar{6}1$	76	1	0.557	x
$634, 9\bar{3}4, 9\bar{6}4$	63	16	0.554	
$219, 3\bar{1}9, 3\bar{2}9$	7	81	0.550	x

[a] Based on space group $P6_322$, a_o = 5.625 Å and c_o = 5.193 Å, from Holmbetg and Dagerhamn, Acta Chem. Scand. 15, 919 (1961).

[b] X-mark denotes superlattice reflections not operable in the α-Zr matrix.

The structure factor of the $(hk\ell)$ plane is given by the equation

$$\begin{aligned} F_{hk\ell} = f_{Zr}\, [1 &+ e^{2\pi i\,(\frac{1}{3}h + \frac{1}{2}\ell)} + e^{2\pi i\,(\frac{1}{3}k + \frac{1}{2}\ell)} \\ &+ e^{2\pi i\,(\frac{2}{3}h + \frac{1}{3}k)} + e^{2\pi i\,(\frac{1}{3}h + \frac{2}{3}k)} + e^{2\pi i\,(\frac{2}{3}h + \frac{2}{3}k + \frac{1}{2}\ell)}] \\ &+ f_{ox}\, [e^{2\pi i\,(\frac{2}{3}h + \frac{1}{3}k + \frac{1}{4}\ell)} + e^{2\pi i\,(\frac{1}{3}h + \frac{2}{3}k + \frac{3}{4}\ell)}]. \qquad (3.1) \end{aligned}$$

In Eq. (3.1), f_{Zr} and f_{ox} are the atomic scattering factors of zirconium and oxygen, respectively, and $(hk\ell)$ represent the Miller indices of the reciprocal lattice point. The structure factor rules for superlattice reflections can be summarized as follows:

$F^*F = 0$, for $h = 3n$, $k = 3m$, and ℓ = odd;

$F^*F = f_{ox}^2$, for $h = 3n$, $k = 3m \pm 1$, and ℓ = even,
$h = 3n \pm 1$, $k = m$, and ℓ = even,
$h = 3n + 1$, $k = 3m - 1$, and ℓ = even,
$h = 3n - 1$, $k = 3m + 1$, and ℓ = even;

and

$F^*F = 3\, f_{ox}^2$, for $h = 3n$, $k = 3m \pm 1$, and ℓ = odd,
$h = 3n \pm 1$, $k = 3m$, and ℓ = odd,
$h = 3n + 1$, $k = 3m - 1$, and ℓ = odd,
$h = 3n - 1$, $k = 3m + 1$, and ℓ = odd,

where n, m, and ℓ are integer numbers. All other cases include f_{Zr} and are not superlattice reflections.

3. Indexing of Zr_3O Superlattice Reflections

Figures 3.1-3.6 show indexed diffraction patterns that contain Zr_3O superlattice reflections. The diffraction patterns in Figs. 3.1 and 3.2 were obtained from within a single grain of the irradiated cladding after fracture and each pattern is characterized by a single major zone of the α-Zr matrix.

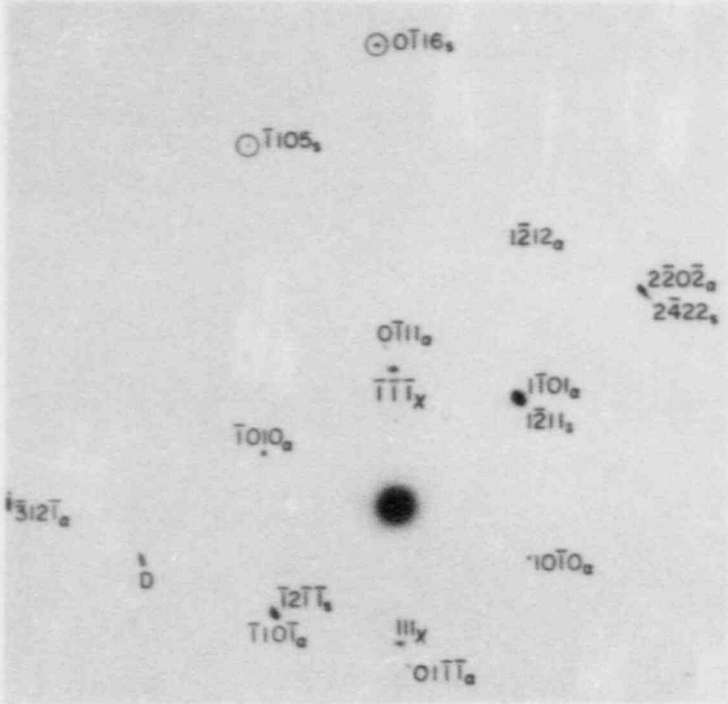

Fig. 3.1. Selected Area Diffraction Pattern Showing Zr$_3$O Superlattice Reflections from a Recrystallized Region Adjacent to the Brittle-Type Failure Site of Specimen 165AE4B. Subscripts α, s, χ, and letter D refer to α-Zr matrix, Zr$_3$O precipitates, χ-hydride, and double diffraction, respectively.

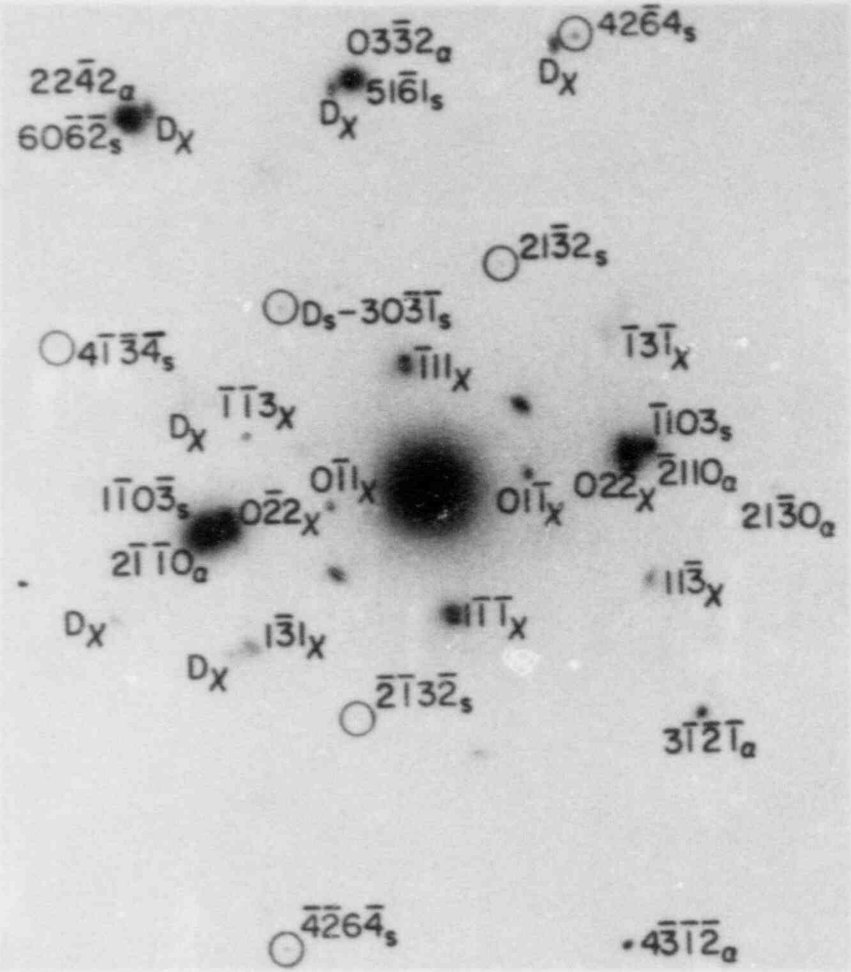

Fig. 3.2. Selected Area Diffraction Pattern Showing Zr$_3$O Superlattice Reflections from a Recrystallized Region Adjacent to the Brittle-Type Failure Site of Specimen 165AE4B. The labeling notations are the same as in Fig. 3.1.

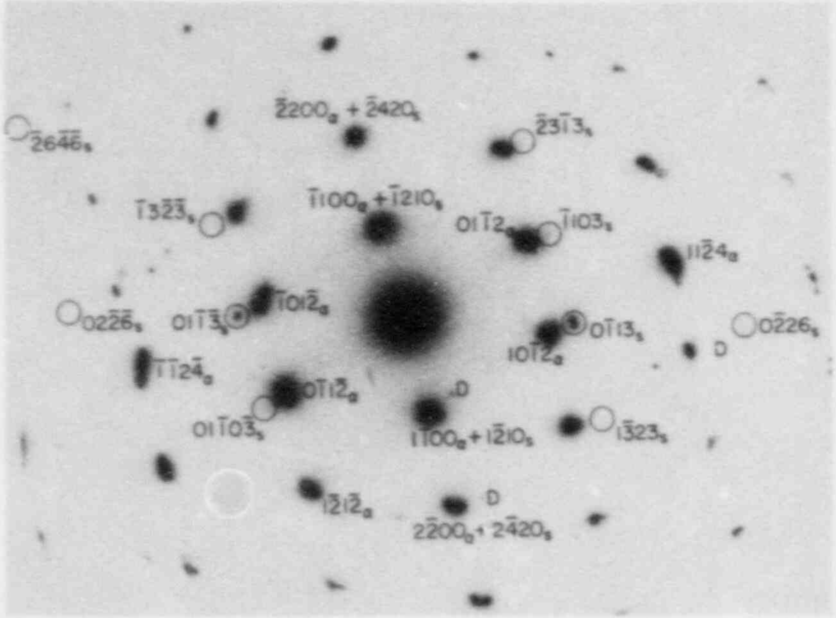

Fig. 3.3. Selected Area Diffraction Pattern Showing Zr_3O Superlattice Reflections from a Cold-worked, Nonrecrystallized Region Adjacent to the Brittle Failure Site of Specimen 165AG10. The labeling notations are the same as in Fig. 3.1.

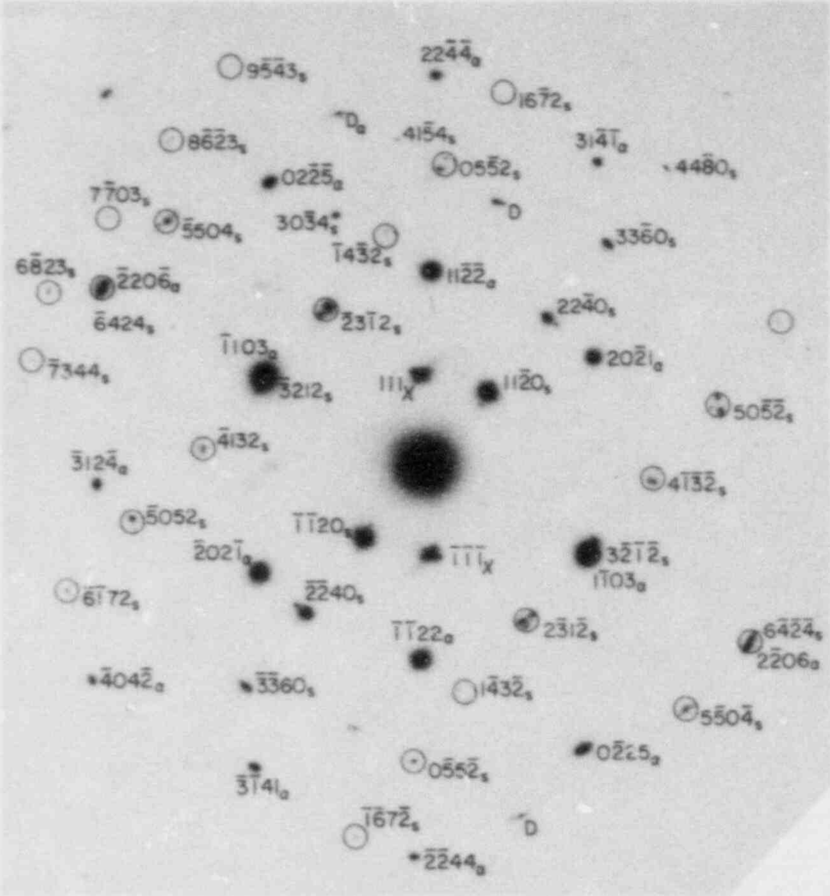

Fig. 3.4. Selected Area Diffraction Pattern Showing Zr_3O Superlattice Reflections of Two Different Zones from a Cold-worked, Nonrecrystallized Region Adjacent to the Brittle Failure Site of Specimen 165AG10. The labeling notations are the same as in Fig. 3.1.

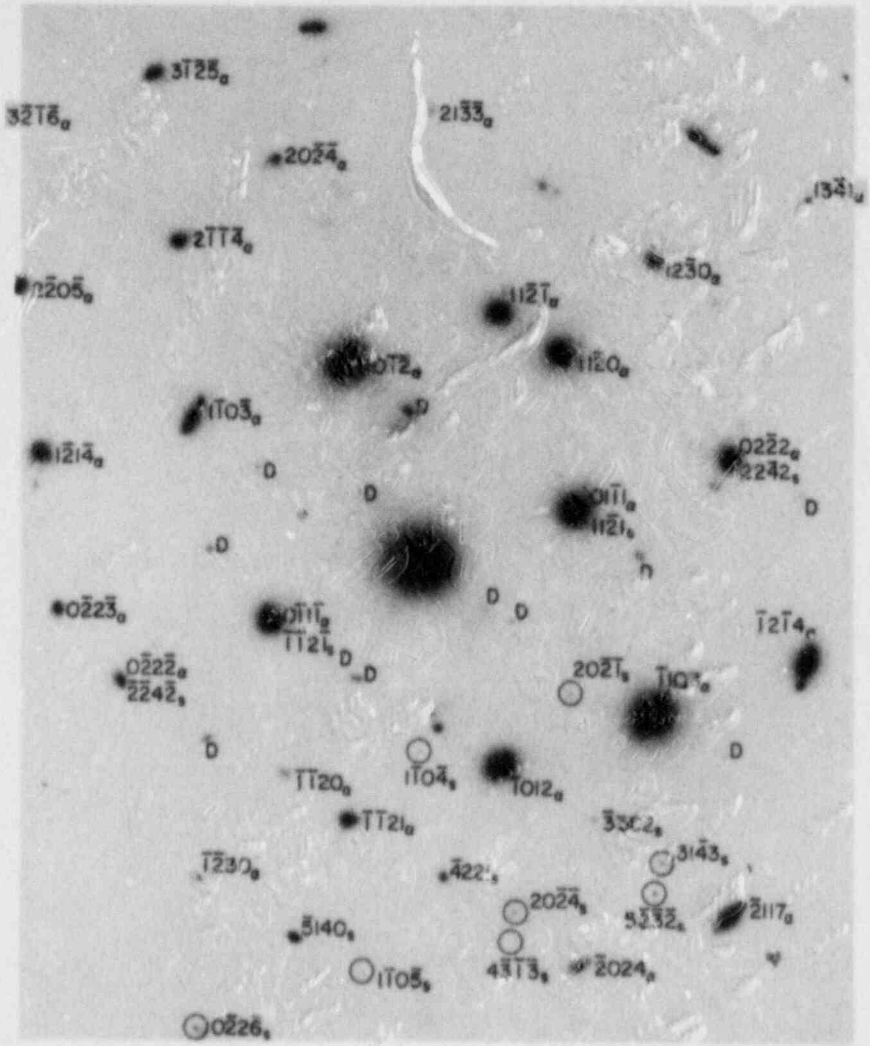

Fig. 3.5. Selected Area Diffraction Pattern Showing Zr_3O Superlattice Reflections of Three Different Zones from a Cold-worked, Nonrecrystallized Region Adjacent to the Brittle Failure Site of Specimen 165AE4B. The labeling notations are the same as in Fig. 3.1.

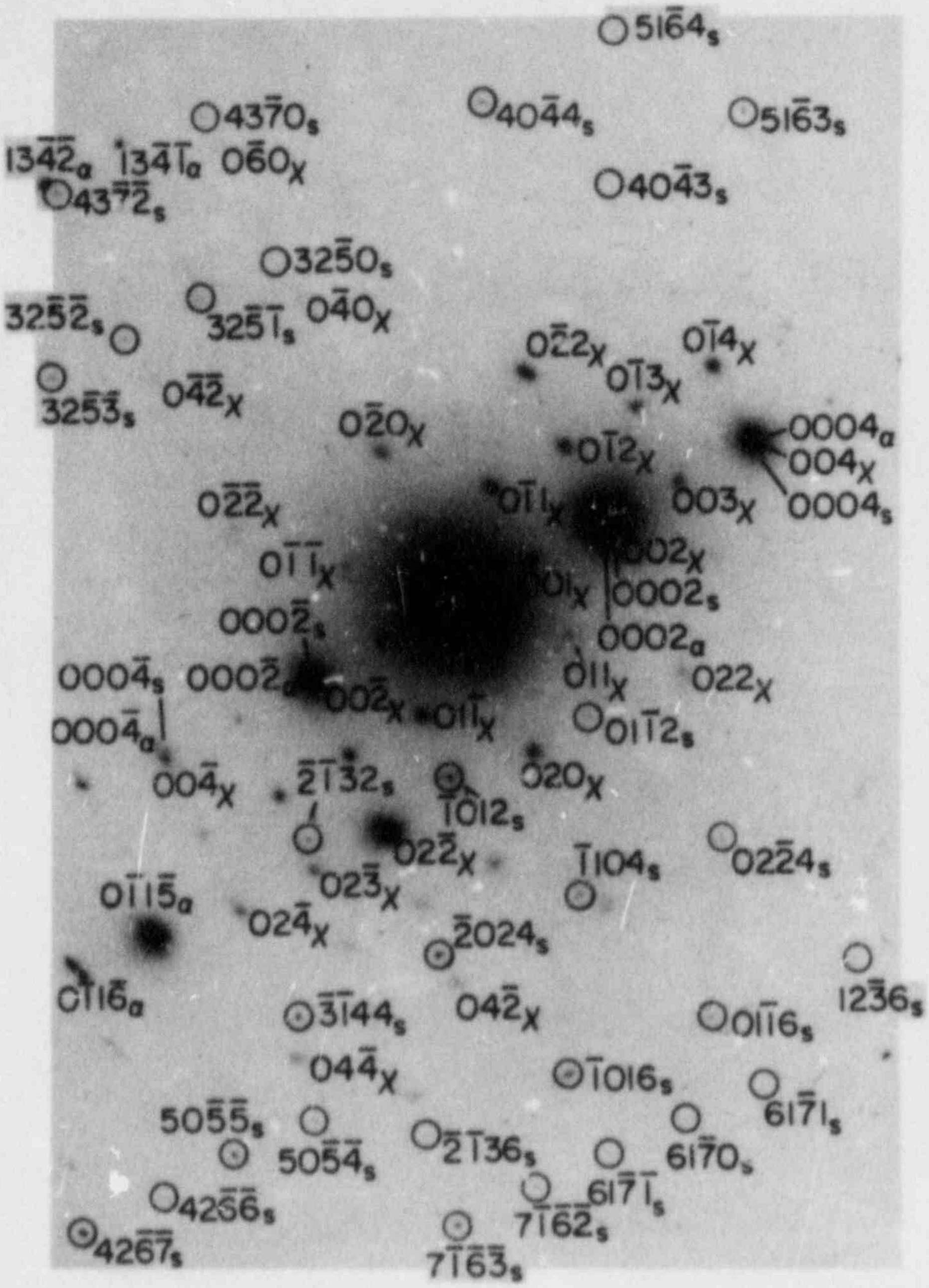

Fig. 3.6. Selected Area Diffraction Pattern Showing Zr$_3$O Superlattice Reflections of Ten Different Zones from a Cold-worked, Nonrecrystallized Region Adjacent to the Brittle Failure Site of Specimen 165AE4B. The labeling notations are the same as in Fig. 3.1.

Diffraction patterns in Figs. 3.3 to 3.6 were obtained from unrecrystallized cold-worked regions and contain multiple zones of not only the α-Zr matrix (α_I phase) but of the Zr_3O phase (α_{II} phase) as well. In the latter figures, as a result of significant relrod* effects, several rows of spots corresponding to different zones are observed usually parallel to a row of strongly reflecting major spots.

Because of the very weak intensity of the superlattice reflections, it is extremely difficult to identify the superlattice spots during the diffraction experiments. They could be identified only after the negatives of the diffraction patterns were developed and indexed. Effort will be devoted to characterize the interaction of the α_{II} phase precipitate with dislocations (or dislocation channels). This can be achieved by examining dark-field morphologies produced from superlattice reflections of the precipitates in association with dislocation substructures.

B. Mandrel Tests on Irradiated Zircaloy Cladding (F. L. Yaggee)

In-reactor PCI-type cladding breaches during normal power transients occur in the vicinity of axial fuel pellet cracks or adjacent to pellet-pellet interfaces. This type of cladding failure, ranging in size from microns to millimeters, also occurs in regions where the cladding microstructure is unable to exhibit a sufficient degree of compliance to the high, local biaxial stress (axial and tangential) imposed by the disparity in thermal expansion between the UO_2 fuel and the Zircaloy cladding. The directional thermal strain differential between the fuel and the cladding is estimated to be 6×10^{-6} and 3.8×10^{-6} $°C^{-1}$ for the axial and tangential directions, respectively.[4] Therefore, a high axial-to-tangential stress ratio can develop in the vicinity of a pellet crack as the result of a high coefficient of friction at the pellet/cladding interface. The axial constraint imposed by pellet/cladding friction or bonding promotes PCI failures by limiting the ability of the mechanically anisotropic cladding to axially comply to the applied tangential stress. Without axial constraint, the cladding contracts axially during tangential expansion. Since the contraction is not allowed under axial constraint, the cladding tends to fail at a smaller tangential strain.

---

*Elongated reciprocal lattice spot due to the very small size of the precipitate phase.

Previous mandrel tests[5,6] on irradiated Zircaloy cladding were conducted in the absence of fission product simulants and without axial specimen constraint. The micron-size breaches occurred at simulated pellet cracks (i.e., the loading ring slit), but at diametral strains of 3 to 4%, which are somewhat larger than the typical diametral strain of a PCI failure. We expect that mandrel expansion tests with axial constraint will result in significantly smaller diametral strains at failure.

A Type 304 stainless steel specimen-constraint fixture was designed and fabricated for use in mandrel tests on the irradiated H. B. Robinson cladding. The vertically split fixture encloses the 50.8-mm-long specimen and provides axial constraint by securing the ends of the specimen with 2.14-mm-diameter Inconel pins. The pins extend through the specimen wall to within 0.2 mm of the inside specimen surface, and are machined concave to blend with the inside specimen radius. A 19.4-mm-long section of the inside diameter of the fixture was enlarged to allow for an 8% specimen diametral strain without obstruction. This approach to specimen axial constraint during mandrel loading tests relies upon close dimensional tolerances between the specimen and fixture (<0.01 mm), reproducibility of the size and spacing of the holes drilled in the specimen, ease of remote assembly and disassembly (especially after thermal cycles between 25 and 325°C), and a significant difference between the axial thermal expansion of specimen and fixture. The difference is about 50% greater than that between the Zircaloy cladding and a UO_2 fuel pellet.[7]

The hardware used to drill the holes in the test specimen and the assembly of the specimen-constraint fixture are illustrated in Figs. 3.7-3.9. Figure 3.7(a) shows the hardened steel die-block used as a guide to drill the holes in the specimen, and a 50.8-mm-long unirradiated Zircaloy specimen to be drilled. The specimen is inserted into the open end of the die-block and the threaded plugs are tightened to capture and center it. The specimen holes are drilled in two operations using a specially ground drill bit. The drilled holes are reamed 0.02 mm larger to remove burrs that may be present after the drilling operation. Figure 3.7(b) shows the drilled specimen after removal from the die-block.

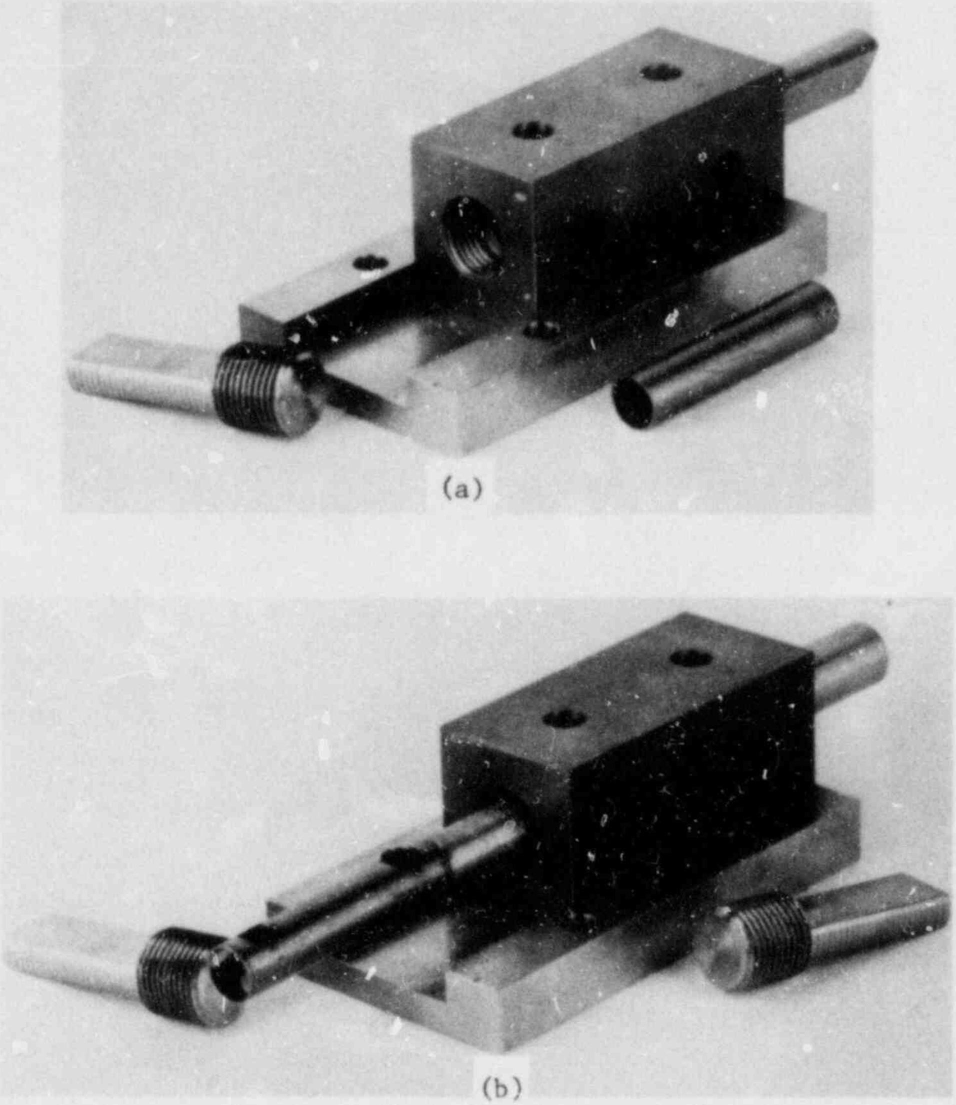

Fig. 3.7. Hardened Steel Die-Block for Drilling Specimen Holes. (a) Die-block open for specimen insertion and (b) specimen with 2.14-mm-diameter drilled holes.

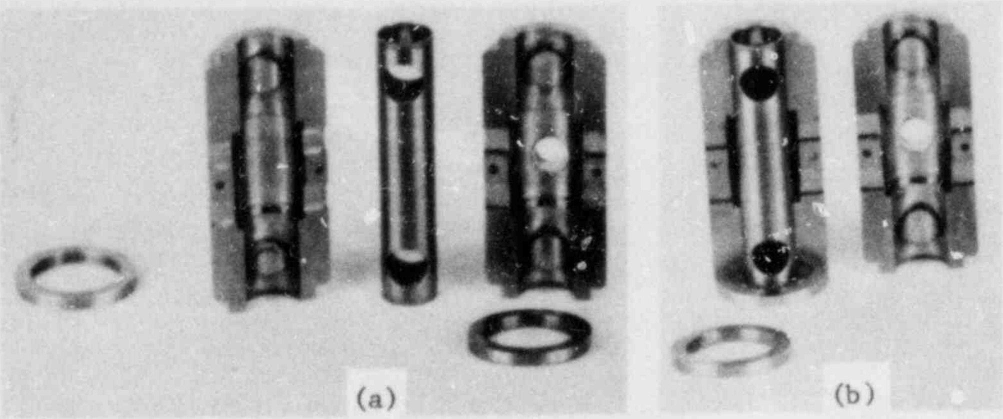
(a) (b)

Fig. 3.8. Axial Constraint Fixture and Specimen. (a) Specimen and fixture components and (b) partial assembly.

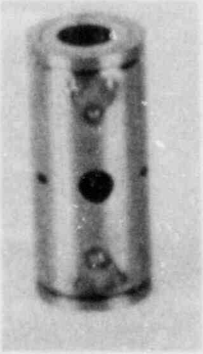

Fig. 3.9. Assembled Fixture Containing Mandrel Specimen.

Figure 3.8 illustrates the assembly of the test specimen within the fixture. The drilled specimen and the components of the fixture are shown in Fig. 3.8(a). The specimen is easily inserted into the back half of the fixture as shown in Fig. 3.8(a). The front half is then pressed in place with a force of <4.5 kg as are the top and bottom retaining rings. Two 0.88-mm-diameter hardened steel pins are inserted to prevent axial displacement between fixture components. The four horizontal slots shown in both halves of the fixture are used to disassemble the fixture with a screwdriver tip after mandrel testing. Figure 3.9 shows the assembled fixture containing the specimen into which the mandrel will be inserted. A 6.4-mm-diameter hole is provided in the front half of the fixture to permit viewing of the portion of the specimen in contact with the split, internal loading ring.

Four unirradiated Zircaloy specimens were drilled successfully and assembled in the fixture to check equipment reliability and the reproducibility of the test procedures. One of these specimens was mandrel loaded at room temperature to a diametral strain of 2.5% to check the axial constraint capability of the fixture. Posttest measurements established no detectable decrease in specimen length or elongation of the holes in the specimen. A mandrel test at 325°C in flowing argon is currently in progress on another unirradiated Zircaloy specimen to check the dimensional stability of the constraining fixture after a 20 to 325°C temperature cycle. The specimen drilling die-block and axial constraint fixture will be introduced into the hot cell for mandrel tests on irradiated cladding after the successful completion of the 325°C mandrel test on unirradiated cladding.

C. References for Chapter III

1. H. M. Chung, in Materials Science and Technology Division Light-Water-Reactor Safety Research Program: Quarterly Progress Report, January-March 1983, NUREG/CR-3689 Vol. I, ANL-83-85, Vol. I (April 1984), pp. 121-135.

2. H. M. Chung, in Materials Science and Technology Division Light-Water-Reactor Safety Research Program: Quarterly Progress Report, April-June 1983, NUREG/CR-3689 Vol II, ANL-83-85 Vol. II (June 1984), pp. 71-79.

3. B. Holmberg and T. Dagerhamn, X-ray Studies on Solid Solutions of Oxygen in α-Zirconium, Acta. Chem. Scand. 15, 919 (1961).

4. MATPRO -- A Handbook of Materials Properties for Use in the Analysis of Light-Water-Reactor Fuel-Rod Behavior, NUREG/CR-0497 (February 1980).

5. F. L. Yaggee, in Materials Science Division Light-Water-Reactor Safety Research Program: Quarterly Progress Report, April-June 1982, NUREG/CR-2970 Vol. II, ANL-82-41 Vol. II (May 1983), pp. 79-96.

6. F. L. Yaggee, in Materials Science and Technology Division Light-Water-Reactor Safety Research Program: Quarterly Progress Report, April-June 1983, NUREG/CR-3689 Vol. II, ANL-83-85 Vol. II (June 1984), pp. 98-113.

7. F. L. Yaggee and F. G. Foote, A Method for Reconstructing a Thermal-Expansion Graph from Two Values of the Mean Expansion Coefficient, ANL-7644 (December 1969).

IV. LONG-TERM EMBRITTLEMENT OF CAST DUPLEX STAINLESS STEELS IN LWR SYSTEMS

Principal Investigators:
O. K. Chopra and W. J. Shack

Progress in this program during the current reporting period is discussed in NUREG/CR-3857 (ANL-84-44).

Distribution for NUREG/CR-3689 Vol. III (ANL-83-85 Vol. III)

Internal:

R. Avery
E. S. Beckjord
O. K. Chopra
H. M. Chung
L. W. Deitrich
C. E. Dickerman
D. R. Diercks
G. R. Fenske
F. Y. Fradin
B. R. T. Frost
E. E. Gruber
G. L. Hofman
M. Ishii
W. D. Jackson
C. E. Johnson
T. F. Kassner (10)
K. L. Kliewer
J. M. Kramer
D. S. Kupperman
D. J. Lam
Y. Y. Liu
P. A. Lottes
P. S. Maiya
D. Moores
K. Natesan
L. A. Neimark
F. A. Nichols
P. R. Okamoto
F. S. Onesto
R. G. Palm
J. Y. Park
R. B. Poeppel
L. E. Rehn
J. Rest (10)
W. E. Ruther
W. J. Shack (3)
E. M. Stefanski (2)
R. V. Strain
C. E. Till
H. C. Tsai
R. A. Valentin
A. Villalobos
R. W. Weeks
H. Wiedersich
F. L. Yaggee
ANL Patent Dept.
ANL Contract File
ANL Libraries (3)
TIS Files (6)

External:

NRC, for distribution per R3 (275)
DOE-TIC (2)
Manager, Chicago Operations Office, DOE
R. Tom, DOE-CH
Materials Science and Technology Division Review Committee:
  B. Alcock, U. Toronto
  A. Arrott, Simon Fraser U.
  R. C. Dynes, Bell Labs., Murray Hill
  A. G. Evans, U. California, Berkeley
  L. M. Falicov, U. California, Berkeley
  H. K. Forsen, Bechtel Group, San Francisco
  E. Kay, IBM San Jose Research Lab.
  B. Maple, U. California, San Diego
  C. L. McCabe, Cabot Corp., Kokomo, Ind.
  P. G. Shewmon, Ohio State U.
  J. K. Tien, Columbia U.
R. B. Adamson, General Electric Co., Vallecitos Nuclear Center, P. O. Box 460, Pleasanton, Calif. 94566
P. L. Andresen, General Electric Corporate Research and Development, Schenectady, N. Y. 12301
G. A. Arlotto, Office of Nuclear Regulatory Research, USNRC, Washington
D. Atteridge, Battelle Pacific Northwest Lab., P. O. Box 999, Richland, Wash. 99352
D. L. Burman, Westinghouse PWR Systems Div., P. O. Box 355, Pittsburgh, Pa. 15230
L. K. Chan, Office of Nuclear Regulatory Research, USNRC, Washington
B. Cox, Chalk River Nuclear Labs., AECL, Chalk River, Ont., K0J 1J0, Canada
R. B. Foulds, Office of Nuclear Reactor Regulation, USNRC, Washington
S. M. Gehl, Electric Power Research Inst., P. O. Box 10412, Palo Alto, Calif. 94304

J. H. Gittus, Springfields Nuclear Power Development Labs., U. K. Atomic Energy
Authority, Springfields, Salwick, Preston, PR4 0RR, England
R. R. Hobbins, EG&G/INEL, 1520 Sawtelle Dr., Idaho Falls, Idaho 83401
W. V. Johnston, Office of Nuclear Reactor Regulation, USNRC, Washington
R. L. Jones, Electric Power Research Inst., P. O. Box 10412, Palo Alto,
Calif. 94304
K. R. Jordan, Nuclear Fuel Div., Monroeville Nuclear Center, Westinghouse
Electric Corp., Monroeville, Pa. 15146
C. N. Kelber, Office of Nuclear Regulatory Research, USNRC, Washington
E. Kohn, Atomic Energy of Canada Ltd., Sheridan Park Research Community,
Mississauga, Ont., Canada L5K 1B2
P. M. Lang, Office of Converter Reactor Deployment, USDOE,
Washington, D. C. 20545
D. D. Lanning, Battelle Pacific Northwest Lab., P. O. Box 999, Richland,
Wash. 99352
R. A. Lorenz, Oak Ridge National Lab., P. O. Box X, Oak Ridge, Tenn. 37830
P. MacDonald, EG&G/INEL, 1520 Sawtelle Dr., Idaho Falls, Idaho 83401
G. P. Marino, Office of Nuclear Regulatory Research, USNRC, Washington
S. McDonald, Westinghouse Electric Corp. R&D Center, Beulah Rd., Pittsburgh,
Pa. 15235
K. R. Merckx, Exxon Nuclear, Inc., 2955 George Washington Way, Richland,
Wash. 99352
A. C. Millunzi, Office of Breeder Reactor Programs, USDOE,
Washington, D. C. 20545
D. R. O'Boyle, Commonwealth Edison Co., P. O. Box 767, Chicago, Ill. 60690
R. N. Oehlberg, Electric Power Research Inst., P. O. Box 10412, Palo Alto,
Calif. 94304
M. F. Osborne, Oak Ridge National Lab., P. O. Box X, Oak Ridge, Tenn. 37830
D. E. Owen, EG&G Idaho, P. O. Box 88, Middletown, Pa. 17057
T. P. Papazoglou, Lynchburg Research Center, Babcock & Wilcox Co., P. O.
Box 1260, Lynchburg, Va. 24505
J. T. A. Roberts, Electric Power Research Inst., P. O. Box 10412, Palo Alto,
Calif. 94304
H. H. Scott, Office of Nuclear Regulatory Research, USNRC, Washington
R. D. Silver, Office of Nuclear Reactor Regulation, USNRC, Washington
P. Smerd, Combustion Engineering, Inc., P. O. Box 500, Windsor, Conn. 06095
A. A. Solomon, School of Nuclear Engineering, Purdue U.,
West Lafayette, Ind. 47907
R. Van Houten, Office of Nuclear Regulatory Research, USNRC, Washington

NRC FORM 335
(2-84)
NRCM 1102,
3201, 3202

U.S. NUCLEAR REGULATORY COMMISSION

BIBLIOGRAPHIC DATA SHEET

SEE INSTRUCTIONS ON THE REVERSE

1. REPORT NUMBER (Assigned by TIDC, add Vol. No., if any)
NUREG/CR-3689 Vol. III
ANL-83-85 Vol. III

2. TITLE AND SUBTITLE
Materials Science and Technology Division Light-Water-Reactor Safety Research Program: Quarterly Progress Report, July—September 1983

3. LEAVE BLANK

4. DATE REPORT COMPLETED
MONTH | YEAR

5. AUTHOR(S)
J. Rest et al.

6. DATE REPORT ISSUED
MONTH: July | YEAR: 1984

7. PERFORMING ORGANIZATION NAME AND MAILING ADDRESS (Include Zip Code)
Argonne National Laboratory
9700 South Cass Avenue
Argonne, Illinois 60439

8. PROJECT/TASK/WORK UNIT NUMBER

9. FIN OR GRANT NUMBER
A2016, A2017, A2212, A2243

10. SPONSORING ORGANIZATION NAME AND MAILING ADDRESS (Include Zip Code)
Division of Engineering Technology
Office of Nuclear Regulatory Research
U. S. Nuclear Regulatory Commission
Washington, D. C. 20555

11a. TYPE OF REPORT
Technical; quarterly

b. PERIOD COVERED (Inclusive dates)
July—September 1983

12. SUPPLEMENTARY NOTES

13. ABSTRACT (200 words or less)

This progress report summarizes the Argonne National Laboratory work performed during July, August, and September 1983 on water reactor safety problems. The research and development areas covered are Environmentally Assisted Cracking in Light Water Reactors, Transient Fuel Response and Fission Product Release, Clad Properties for Code Verification, and Long-Term Embrittlement of Cast Duplex Stainless Steels in LWR Systems.

14. DOCUMENT ANALYSIS – a. KEYWORDS/DESCRIPTORS
fission product modeling
fission product release
irradiated Zircaloy cladding
mandrel load tests
Zircaloy fracture
Zr_3O precipitation

b. IDENTIFIERS/OPEN-ENDED TERMS

15. AVAILABILITY STATEMENT
unlimited

16. SECURITY CLASSIFICATION
(This page)
unclassified
(This report)
unclassified

17. NUMBER OF PAGES

18. PRICE

120555078877 1 IAN1R3
US NRC
ADM-DIV OF TIDC
POLICY & PUB MGT BR-PDR NUREG
W-501
WASHINGTON DC 20555